Oligomeric Semiconductors Enable High Efficiency Open Air Processed Organic Solar Cells by Modulating Pre-aggregation and Crystallization Kinetics

Hao Xia,[a,b] Ying Zhang,*[b] Kuan Liu,[b] Wanyuan Deng,[c] Mengbing Zhu,[a] Hua Tan,[a] Patrick W K Fong,[b] Heng Liu,[d] Xinxin Xia,[d] Miao Zhang,[e] Top Archie Dela Peña,[fgh] Ruijie Ma,[b] Mingjie Li,[g] Jiaying Wu,[f] Yongwen Lang,[b] Jiehao Fu,[b] Wai-Yeung Wong,[e] Xinhui Lu,[d] Weiguo Zhu,*[a] Gang Li*[b]

[a]*School of Materials Science and Engineering, Jiangsu Engineering Laboratory of Light-Electricity-Heat Energy-Converting Materials and Applications, Jiangsu Collaborative Innovation Center of Photovoltaic Science and Engineering, National Experimental Demonstration Center for Materials Science and Engineering, Changzhou University, Changzhou 213164, China.*
[b]*Department of Electronic and Information Engineering, The Hong Kong Polytechnic University, Hung Hum Kowloon, Hong Kong 999077, China*
[c]*State Key Laboratory of Luminescent Materials and Devices, Institute of Polymer Optoelectronic Materials and Devices, South China University of Technology, Guangzhou 510640, China*
[d]*Department of Physics, The Chinese University of Hong Kong, New Territories, Hong Kong 999077, China*
[e]*Department of Applied Biology and Chemical Technology, The Hong Kong Polytechnic University, Hung Hum Kowloon, Hong Kong 999077, China*
[f]*The Hong Kong University of Science and Technology, Function Hub, Advanced Materials Thrust, Nansha 511400, Guangzhou, P. R. China*
[g]*The Hong Kong University of Science and Technology, School of Science, Department of Chemistry, Kowloon, Hong Kong 999077, P.R. China*
[h]*The Hong Kong Polytechnic University, Faculty of Science, Department of Applied Physics, Kowloon, Hong Kong 999077, P.R. China;*

Email addresses:
Yingeva.zhang@polyu.edu.hk
zhuwg18@126.com(W.Z.)
gang.w.li@polyu.edu.hk (G.L.)

Abstract:

Although massive progress in power conversion efficiencies (PCEs) has been made on organic solar cells (OSCs), the challenge remains to scale up high-performance OSCs that are compatible with the industrial production conditions, i.e. post-treatment-insensitive, non-halogenated solvent, large area printing, processing under atmospheric environment, etc. In this work, two A-D-A-D-A type oligomers, named 5BDDBDT-F and 5BDDBDT-Cl, were designed and synthesized to be incorporated into binary OSCs. Ex situ and in situ characterizations are performed to unveil the underlying working mechanisms. The two-phase transitions: liquid-to-liquid and liquid-to-solid can be synergistically tailored to promote the molecular arrangement of the binary blend. Benefiting from the enhanced crystallinity, oligomer can act as a bridging linker to rehabilitate the interfacial defects to reduce the trap-assisted recombination losses and thus the non-radiative recombination losses. As a result, using non-halogenated solvent (*o*-xylene), the best-performing OSCs with PCEs of 18.32% with a V_{OC} of 0.850 V, a FF of 79.15% were achieved based on the PM6:5BDDBDT-F:BTP-eC9 ternary OSCs, and 18.43% with a V_{OC} of 0.854 V, a FF of 79.29% were obtained based on PM6:5BDDBDT-Cl:BTP-eC9 ternary OSCs without any post-processing. More importantly, it is noteworthy that the large-area (1 cm^2) blade coated devices based on PM6:5BDDBDT-F:BTP-eC9 and PM6:5BDDBDT-Cl:BTP-eC9, processed using non-halogenated solvent in an open-air environment without thermal-annealing treatment, obtained a high PCE of 17.11% and 17.06%, respectively, which are among the highest PCE values of blade-coated OSCs in open air. This work demonstrated an efficient strategy of controlling crystallization kinetics to improve the material crystallinity, as an effective guideline for achieving high photovoltaic performance in printing ternary OSCs, pushing the OSCs towards future manufacturing.

KEYWORDS: Oligomer donors; Organic solar cells; Crystallinity regulation; Green solvent processing; Blade coating large area;

1. Introduction

Organic solar cells (OSCs), one of the most potential photovoltaic (PV) technologies, have distinct advantages such as light-weight, flexibility, semitransparency and large-scale roll-to-roll processing.[1-4] Up to date, OSCs have developed rapidly over the past few decades with power conversion efficiencies (PCEs) surpassing 19%,[5-10] which is closely intertwined with the innovation of materials, device engineering, and device physical mechanisms.[11-14] However, these breakthroughs are mostly made in halogenated solvent-processed (e.g., chlorobenzene, chloroform, etc.) OSCs devices are typically with extra steps of post-treatments, such as thermal annealing (TA) [15-17] and solvent vapor annealing (SVA),[18-20] which is not favorable for large-area manufacturing. Therefore, device optimization with a focus on the morphology manipulation of green solvents-processed devices is crucial to push OSCs to the next stage. Some attempts, including synthesizing novel materials,[21,22] adopting green additives,[23,24] and utilizing new film structures,[25] have been made to improve the performances of non-halogenated solvents processed OSCs.

Besides the methods above, it is well established that the ternary strategy is also an effective and feasible way to finely tune active layer morphology and improve OSCs performance.[26-30] Previous works have demonstrated that the pre-aggregation kinetics in a liquid state as well as phase transition kinetics from solution state to solid state is critical for the final film morphology.[31] However, active layer microstructure optimization and device performance correlation lack the fundamental understanding of the effects of the third component on the film formation kinetics, and is almost always a process of trial and error so far.[32-34] Therefore, it is very important to get an in-depth investigation of structural evolution and clarify the desired morphology formation during the whole optimal film formation stages - evolving from solution state, spin coating-induced frozen state, to TA processes.

Recently, there have been many efforts on revealing the relationship between morphology and photo-physics including charge generation, charge transport, and recombination. Hou and coworkers[35] demonstrated that optimizing the vertical phase

separation by adding the third component can suppress the trap state density, which contributes to enhanced device performance. Jen et al.[8] reported the bimolecular recombination can be mitigated by successfully constructing the mixed-planar heterojunction structure (MPHJ), leading to the ultrafast charge transfer and higher carrier densities and thus the higher J_{SC}. However, the investigations of correlation among the morphology formation-physical mechanism-device performance are an important step for the industrial up-scalable printing process.

Recently, we discovered an oligomer 5BDDBDT can boost the V_{OC} in OPV, through reducing the non-radiative energy loss in OSCs. In this work, two oligomers of type A-D-A-D-A, named 5BDDBDT-F and 5BDDBDT-Cl, were further designed and synthesized with significantly reduced HOMO level values compared to 5BDDBDT.[36,37] The ternary OSCs based on the PM6:5BDDBDT-F:BTP-eC9 and PM6:5BDDBDT-Cl:BTP-eC9 blend were constructed. Ex situ and in situ characterizations of the morphology further reveal that the oligomers could promote two phase transitions kinetics: pre-aggregation and crystallization. The host donors and acceptors both show much improved crystallinity in the ternary systems, which helps to achieve lower trap state densities and lower non-radiative recombination losses compared to binary systems, and thus enhanced device efficiency. In addition, we reveal that the effect on the morphology evolution in naturally dried and thermally annealed films is different, while the first one enhances crystallinity and the TA relaxes aggregates. As a result, using non-halogenated solvent (*o*-xylene), the best performing OSC with PCEs of 18.32% with a V_{OC} of 0.850 V, a FF of 79.15% was achieved based on the PM6:5BDDBDT-F:BTP-eC9 ternary OSCs, and 18.43% with a V_{OC} of 0.854 V, a FF of 79.29% was obtained based on PM6:5BDDBDT-Cl:BTP-eC9 ternary OSCs, both without any post-processing. Furthermore, it is noteworthy that the large-area (1 cm^2) blade coating devices based on PM6:5BDDBDT-F:BTP-eC9 and PM6:5BDDBDT-Cl:BTP-eC9, processed using non-halogenated solvent in an open-air environment without the TA treatment, still obtained a high PCE of 17.11% and 17.06%, respectively, which are among the highest PCE values of blade-coating OSCs processed in open air. Importantly, these PCE values have been independently certified at 17.22%

and 17.37%. Therefore, rational oligomer incorporation is an efficient strategy in controlling materials crystallization, which is of great desire for achieving high performance printing friendly OSCs.

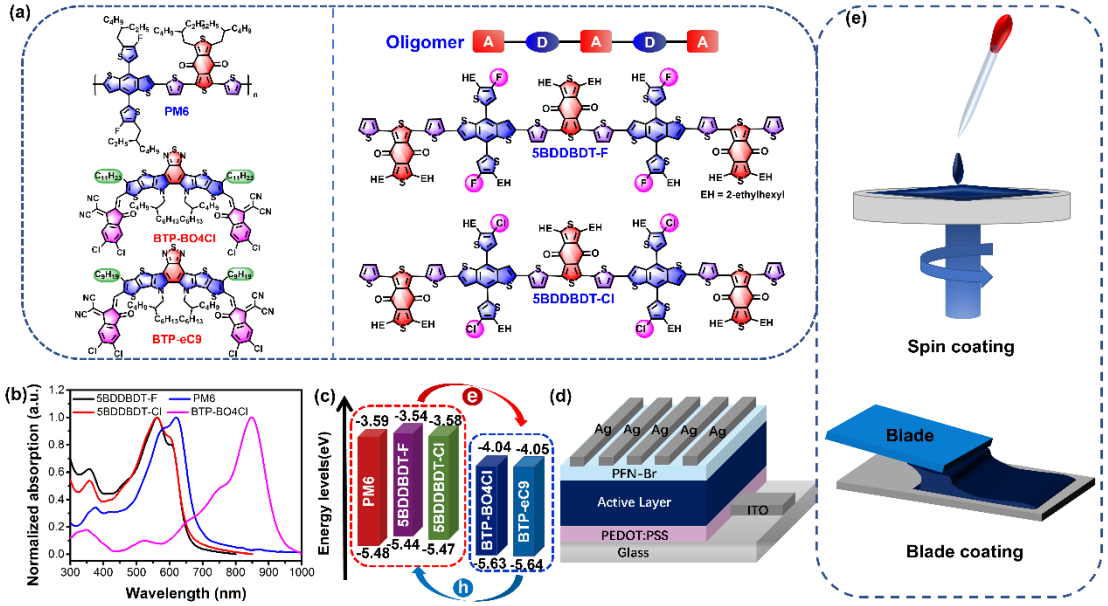

Figure 1. a) Chemical structures of PM6, BTP-BO4Cl, BTP-eC9, 5BDDBDT-F and 5BDDBDT-Cl. b) Normalized UV-vis absorption spectra in neat films. c) Energy levels of PM6, 5BDDBDT-F, 5BDDBDT-Cl, BTP-BO4Cl and BTP-eC9. d) Schematic diagram of the conventional device structure. e) Schematic diagram of spin coating and blade coating procedure.

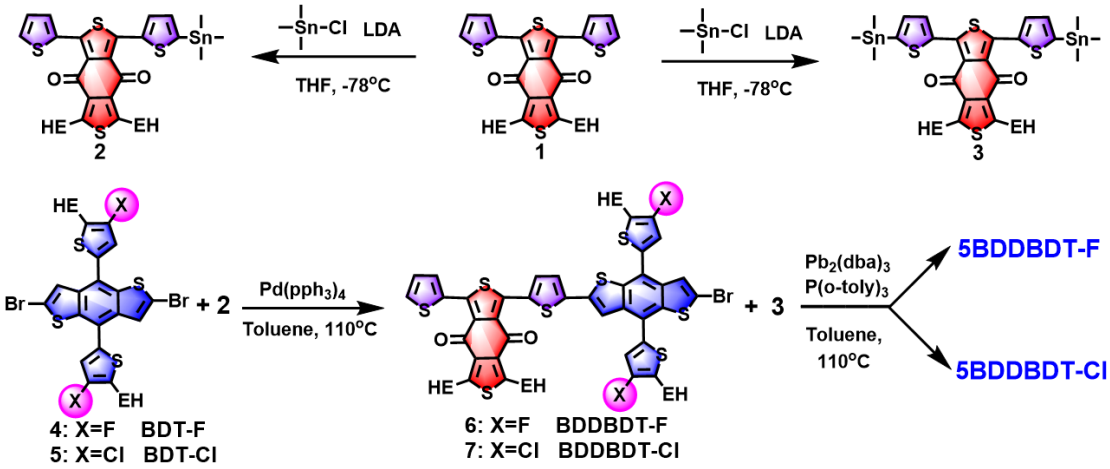

Scheme 1. Synthetic routes for oligomer 5BDDBDT-F and 5BDDBDT-Cl.

2. Results and Discussion

Synthesis, Optical and Electrochemical Properties

The synthetic routes of 5BDDBDT-F and 5BDDBDT-Cl are described in **Scheme 1**.

The synthesis method of compound 2 and 3 can refer to the previous literature.[37] Compounds 6 and 7 were synthesized by one-sided Stille coupling of compounds 4 and 5 to compound 2, respectively. 5BDDBDT-F and 5BDDBDT-Cl were obtained by a Stille two-sided coupling reaction of 6 and 7 with 3, respectively. All synthetic details are depicted in Electronic Supporting Information (ESI). Moreover, all products are fully characterized by ^{1}H NMR. In addition, ^{13}C NMR and MALDITOF-MS were used to characterize the end products. The oligomers 5BDDBDT-F and 5BDDBDT-Cl show good solubility in common solvents (such as chlorobenzene, *o*-xylene, dichloromethane, and chloroform).

The UV–Vis absorption spectra of oligomer donors 5BDDBDT-F, 5BDDBDT-Cl, polymer PM6 and acceptor BTP-BO4Cl were investigated in dilute *o*-xylene solution (10^{-5} mol L^{-1}) and neat films, shown in **Figure 1b** and Figure S1(a), respectively, and the relevant optical data are listed in **Table 1**. As shown in Figure S1, the absorption spectra of both oligomers obviously exhibit a 50 nm redshift from solution to thin film due to their closer intermolecular interaction. Moreover, the absorption spectra of 5BDDBDT-F and 5BDDBDT-Cl are slightly blue-shifted from PM6, suggesting that the mixed absorption spectrum can better cover the 300-1000 nm range. The optical band gaps (E_g^{opt}) of 5BDDBDT-F, 5BDDBDT-Cl and PM6 are estimated as 1.89, 1.90 and 1.81 eV, respectively, according to the empirical formula (E_g^{opt} =1240/λ_{onset}). Additionally, the absorption spectra of the blended films with and without TA are provided in Figure S1b. The absorption of the blended film after TA shows a slight redshift compared to that before TA, and its extinction coefficient is also slightly increased, implying that the TA setup may be able to obtain a larger J_{SC}.

The energy levels of pure donor and acceptor were measured using the cyclic voltammetry (CV) measurements (Figure S2, Supporting Information), and the relative data are shown in **Table 1**. The highest occupied molecular orbital (HOMO) and lowest unoccupied molecular orbital (LUMO) values of 5BDDBDT-F, 5BDDBDT-Cl and PM6 were calculated as -5.44, -5.47, -5.48 eV, and 3.53, 3.58, 3.59 eV, respectively. Obviously, 5BDDBDT-F and 5BDDBDT-Cl oligomers exhibit decreased HOMO

levels, due to the electronegativity of F and the empty 3d orbital of Cl, when compared with our previously reported oligomer 5BDDBDT,[36,37] but still higher than PM6 (-5.48 eV). Moreover, both PM6:5BDDBDT-F:BTP-BO4Cl and PM6:5BDDBDT-Cl:BTP-BO4Cl systems exhibit cascade-like energy level alignment, as shown in **Figure 1c**, which would promote charge transfer and transport in the ternary blend.[38,39]

The geometries, energy levels and wave functions of 5BDDBDT-F, 5BDDBDT-Cl were investigated by the density functional theory (DFT) at the B3LYP/6–31G* basis set using Gaussian 09W program, as shown in Figure S3 in the Supporting Information. All the alkyl side chains in the molecules are replaced by methyl groups to simplify the calculations. As a result, the molecular backbones of both oligomers display excellent planarity, which facilitates intermolecular π-π stacking and promotes charge transport. In addition, 5BDDBDT-Cl shows deeper HOMO and LUMO levels compared to 5BDDBDT-F due to the empty 3d atomic orbitals of Cl, which is consistent with the CV results. This implies that higher V_{OC} may be obtained for devices based on the 5BDDBDT-Cl.

Table 1. Optical and electrical properties of 5BDDBDT-F, 5BDDBDT-Cl and PM6 films.

Donor	λ_{max} (nm)		$\lambda_{onset.film}$	E_g^{opt}	E_{HOMO}	E_{LUMO}
	Solution	Film	(nm)	(eV)[a]	(eV)[b]	(eV)[b]
5BDDBDT-F	512	563, 603	655	1.89	-5.44	-3.53
5BDDBDT-Cl	511	561, 599	653	1.90	-5.47	-3.58
PM6	550	580, 620	684	1.81	-5.48	-3.59

[a]Calculated from the absorption band edge of the films, $E_g^{opt} = 1240/\lambda_{onset}$
[b]Calculated from empirical equation: $E_{HOMO/LUMO} = -(E_{ox/red} + 4.8)$ eV (The formal potential of Fc/Fc^+ is 0.43 V *vs*. Ag/AgCl measured in this work)

Photovoltaic Properties

To estimate the photovoltaic performance of new oligomers, ternary OSCs were fabricated with a device structure (**Figure 1d**) of ITO/PEDOT:PSS/Active layer/PFN-Br/Ag. The detailed device preparation process is presented in the Supporting Information. All devices were fabricated in the optimal processing condition with the D:A weight ratio of 1:1.2 using *o*-xylene (XY) as the processing solvent with 0.5%

additive of 1,8-diiodooctane (DIO). **Figure 2a** shows the current density–voltage (*J–V*) curves of the best-performing binary and ternary devices under the illumination of AM 1.5G, 100 mW cm^{-2} with or without post-treatment, and the corresponding performance parameters are summarized in **Table 2**. Both 5BDDBDT-F and 5BDDBDT-Cl were found to have the optimized weight ratios at ca. 10 wt%. With a TA treatment of 100 ºC for 10 min, PM6:5BDDBDT-F:BTP-BO4Cl-based and PM6:5BDDBDT-Cl:BTP-BO4Cl-based ternary devices obtain PCEs of 17.25% with a V_{OC} of 0.840 V, a FF of 77.88%, and a PCE of 17.26% with a V_{OC} of 0.846 V, a FF of 78.19%, respectively, which are obvious higher than the control device (PM6:BTP-BO4Cl) of 16.41%, which is consistent with the related reported results.[40] Excitingly, without TA treatment, PM6:5BDDBDT-F:BTP-BO4Cl-based and PM6:5BDDBDT-Cl:BTP-BO4Cl-based ternary devices obtained impressive PCEs of 17.16% with a V_{OC} of 0.846 V, a FF of 78.04%, and PCE of 17.35% with a V_{OC} of 0.857 V, a FF of 78.03%, which are obviously higher than the control devices (PCE of 16.26% with a V_{OC} of 0.840 V, a FF of 74.93%). In addition, we also prepared blade coating devices based on PM6:5BDDBDT-F:BTP-BO4Cl and PM6:5BDDBDT-Cl:BTP-BO4Cl using *o*-xylene as processing solvent in an atmospheric environment to simulate industrial production conditions. The 5BDDBDT-F and 5BDDBDT-Cl-based ternary small area blade coating devices achieved an impressive performance of PCE of 17.13% with FF of 78.36% and a PCE of 17.15% with FF of 78.25% without post-treatment, respectively, as shown in Figure S4 and Table S1. Notably, when the active layers were treated with TA (100 °C, 10 min), both control and ternary blade coating devices showed a lower FF than untreated devices. Nevertheless, under thermal annealing, the ternary device exhibited higher FF than the control. The results show that the addition of a small content of oligomers could improve the device's tolerance to thermal stress and optimize the morphology of the active layer, which will be discussed in later sections. Such molecules could help to fulfill industrial requirements and facilitate the manufacturing of organic solar cells. The external quantum efficiencies (EQEs) spectra of control, PM6:5BDDBDT-F:BTP-BO4Cl-based, PM6:5BDDBDT-Cl:BTP-BO4Cl-based devices were measured accordingly. As shown in **Figure 2b**, **2e** and **2h**, all curves

reveal a similar shape and overlap the spectrum range from 300-950 nm. The optimal devices without TA will lead to a blue-shifted absorption edge, resulting in a slight decreased J_{SC}, but a higher V_{OC}.

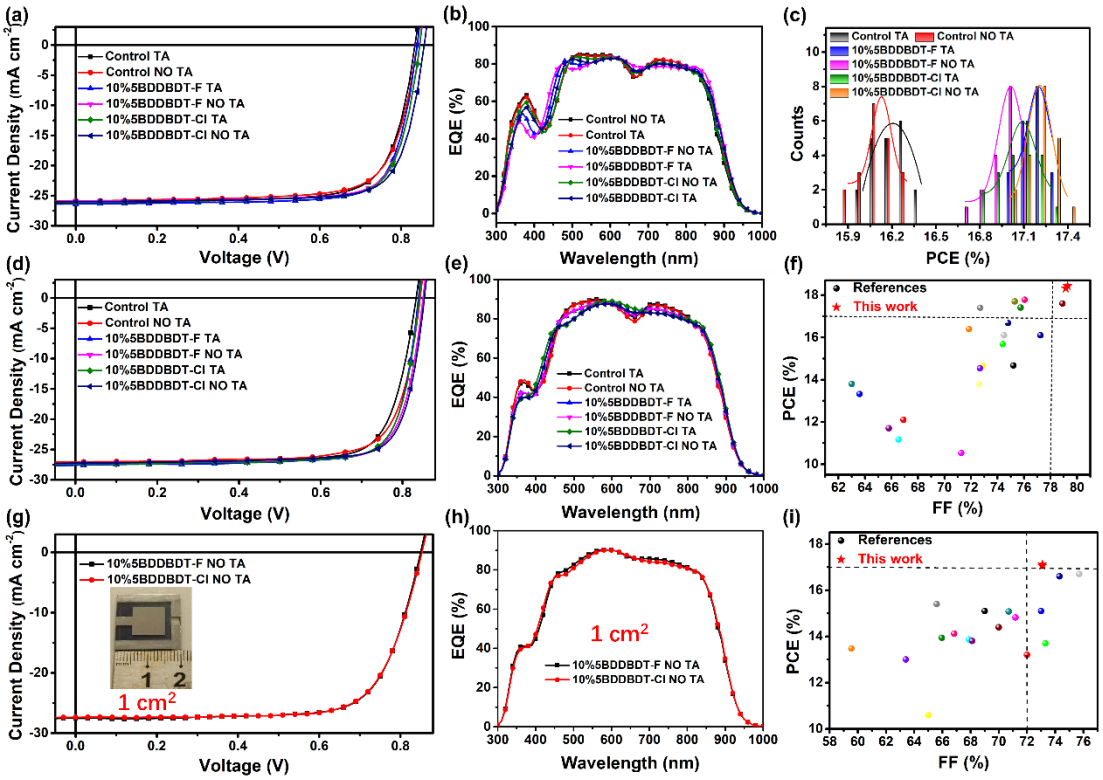

Figure 2. a) *J–V* curves, b) EQE spectra and c) Histogram of PCE counts of the optimal control, 10%5BDDBDT-F and 10%5BDDBDT-Cl spin coating devices based on PM6:oligomer:BTP-BO4Cl system. d) *J–V* curves and e) EQE spectra of the optimal control, 10%5BDDBDT-F and 10%5BDDBDT-Cl spin coating devices based on PM6:oligomer:BTP-eC9 system. f) Summary FF and PCE of the spin coating OSCs without post-treatment in the literature (PCE > 10%) and this work (the related references are listed in Table S2 and cited in the ESI†). g) *J–V* curves and h) EQE spectra of 10%5BDDBDT-F and 10%5BDDBDT-Cl 1 cm^2 area ternary blade coating devices without post-treatment. i) Summary FF and PCE of the 1 cm^2 area blade coating OSCs in the literature (PCE > 10%) and this work (the related references are listed in Table S3 and cited in the ESI†).

Table 2. The photovoltaic parameters of the binary and ternary small area spin coating devices based on PM6:BTP-BO4Cl system with and without TA.

Third component ratio	Treatment	V_{OC} (V)	J_{SC}[a] (mA cm^{-2})	J_{SC}^{EQE} (mA cm^{-2})	FF (%)	PCE_{max}[b] (%)
0%[c]	TA	0.834	26.12	25.45	75.21	16.41 16.22±0.12
	NO TA	0.840	25.83	25.34	74.93	16.26 16.15±0.13
10%5BDDBDT-F[c]	TA	0.840	26.37	25.52	77.88	17.25 17.17±0.09

	NO TA	0.846	25.98	25.38	78.04	17.16 17.07±0.14
10%5BDDBDT-Cl[c]	TA	0.846	26.13	25.26	78.19	17.26 17.06±0.17
	NO TA	0.857	25.95	25.12	78.03	17.35 17.21±0.16

[a]J_{SC} measured from devices. [b]PCE obtained from 20 devices, [c]D:A = 10:12 mg/ml, with 0.5% DIO additive.

Table 3. The photovoltaic parameters of the binary and ternary blade coating devices based on PM6:BTP-eC9 with and without TA.

Third component ratio	Coating method	Area (cm^2)	Treatment	V_{OC} (V)	J_{SC}[a] (mA cm^{-2})	J_{SC}^{EQE} (mA cm^{-2})	FF (%)	PCE_{max}[b] (%)
Control[c]	Spin coating	0.042	TA	0.833	27.52	26.57	76.35	17.50 17.35±0.14
	Spin coating	0.042	NO TA	0.843	27.09	26.23	76.34	17.43 17.30±0.13
10%5BDDBDT-F[c]	Spin coating	0.042	TA	0.839	27.58	26.34	79.00	18.28 18.09±0.11
	Spin coating	0.042	NO TA	0.850	27.24	26.21	79.15	18.32 18.17±0.14
	Blade coating	1	NO TA	0.850	27.54	26.89	73.09	17.11
	Blade coating[d]	1	NO TA	0.846	27.62	--	73.70	17.22
10%5BDDBDT-Cl[c]	Spin coating	0.042	TA	0.841	27.37	26.43	79.12	18.21 18.12±0.18
	Spin coating	0.042	NO TA	0.854	27.22	26.20	79.29	18.43 18.26±0.15
	Blade coating	1	NO TA	0.853	27.37	26.78	73.08	17.06
	Blade coating[d]	1	NO TA	0.850	27.57	--	74.13	17.37

[a]J_{SC} measured from devices. [b]PCE obtained from 15 devices. [c]D:A = 10:12 mg/ml, with 0.5% DIO additive. [d]Device performance certified at the City University of Hong Kong.

Charge Separation, Transport and Recombination

Since the improvement in PCE for these ternary OSCs is mainly attributed to the improvements in J_{SC} and FF, we analyze the exciton dissociation, charge transfer and collection in devices. The dependence between the photocurrent density (J_{ph}) and effective voltage (V_{eff}) was first researched, as shown in **Figure 3a**. Here, $J_{ph} = J_L - J_D$, where J_L and J_D are the current densities under illumination and darkness, respectively. In addition, $V_{eff} = V_0 - V_{appl}$, where V_0 is the voltage when $J_L = J_D$, and V_{appl} is the applied bias voltage. When the V_{appl} is high enough ($\geq$ 2 V), all the excitons are separated into free carriers, and J_{ph} reaches a saturation state (J_{sat}). Hence, the efficiency of exciton dissociation (η_{diss}) or charge collection (η_{coll}) can be defined as the J_{ph}/J_{sat} values under short circuit conditions or maximum power output conditions, respectively.[41] The η_{diss} and η_{coll} of PM6:5BDDBDT-F:BTP-BO4Cl (97.41% and 88.05%) and PM6:5BDD-BDT-Cl:BTP-BO4Cl ternary OSCs (97.49% and 88.27%) with TA are slightly higher than of PM6:BTP-BO4Cl (96.78% and 87.74%). Similarly, the ternary OSCs based on 5BDDBDT-F and 5BDDBDT-Cl exhibit a higher η_{diss} (97.55%

and 97.67%) and η_{coll} (89.08% and 89.30%) value compared with η_{diss} (97.45%) and η_{diss} (88.62%) of control binary OSCs without the TA treatment, indicating the more efficient exciton dissociation, charge transport and collection efficiency in ternary OSCs either after with TA or without TA treatment.

In order to understand the charge transfer situation in these binary and ternary devices, steady-state photoluminescence (PL) spectra were measured. The PM6 maximum absorption peak is blue-shifted by 20 nm corresponding to the wavelength of the light used to excite the PM6 neat film, PM6:BTP-BO4Cl, PM6:5BDDBDT-F:BTP-BO4Cl and PM6:5BDDBDT-Cl:BTP-BO4Cl blend films. As shown in Figure S5, strong PL intensity is observed in the PM6 neat film, and it quenched in the PM6:BTP-BO4Cl, PM6:5BDDBDT-F:BO4Cl and PM6:5BDDBDT-Cl:BTP-BO4Cl blend films with high quenching efficiencies of 95.44%, 98.12% and 96.47%, respectively. Moreover, the emission of the 5BDDBDT-F and 5BDDBDT-Cl neat films are also quenched in the blend films of PM6:5BDDBDT-F:BTP-BO4Cl and PM6:5BDDBDT-Cl:BTP-BO4Cl with high quenching efficiencies of 93.43% and 95.33% (Figure S5b and S5c), respectively. The above PL test results indicate that ternary blend films exhibit a highly effective charge transfer than binary blend films.[42]

In addition, space-charge limited current (SCLC) method was carried on to evaluate the charge transport properties of the binary and ternary blends (**Figure 3d**, Figure S6).[43] The structures of the electron-only and hole-only devices are ITO/ZnO/Active Layer/PFN-Br/Ag and ITO/PEDOT:PSS/Active Layer/MoO_3/Ag, respectively. For the PM6:BTP-BO4Cl binary blend film, electron (μ_e) and hole (μ_h) mobilities were estimated to be 1.83×10^{-4} cm^2 V^{-1} s^{-1} and 1.02×10^{-4} cm^2 V^{-1} s^{-1} with TA treatment, and 1.35×10^{-4} cm^2 V^{-1} $s^{-1}$and 1.35×10^{-4} cm^2 V^{-1} s^{-1} without TA treatment, respectively. After adding 10%5BDDBDT-F and 10%5BDDBDT-Cl, the μ_h increased to 1.09×10^{-4} cm^2 V^{-1} s^{-1} and 1.26×10^{-4} cm^2 V^{-1} s^{-1} with TA treatment, and 1.42×10^{-4} cm^2 V^{-1} s^{-1} and 1.47×10^{-4} cm^2 V^{-1} s^{-1} without TA treatment, respectively. However, the μ_e slight decreased to 1.61×10^{-4} cm^2 V^{-1} s^{-1} and 2.00×10^{-4} cm^2 V^{-1} s^{-1} with TA treatment, and increase to 1.38×10^{-4} cm^2 V^{-1} s^{-1} and 1.57×10^{-4} cm^2 V^{-1} s^{-1} without TA treatment, respectively. Therefore, the μ_h/μ_e ratio of control, 5BDDBDT-F-based and 5BDDBDT-Cl-based ternary devices were 1.79, 1.48, 1.59 with TA and 1.00, 0.97, 1.07 without TA

treatment, respectively. As shown in **Figure 3d** and Table S4, when oligomer 5BDDBDT-F or 5BDDBDT-Cl is added, the enhancement of μ_h and more balanced μ_h/μ_e are responsible for the enhanced FF in an optimal ternary device. Among them, the significant increase for μ_h in ternary devices, especially in the ternary devices without TA treatment, is attributed to the third component oligomers, which may facilitate the self-assembly of the donor phase and thus promote the hole transport.[44] Moreover, compared with the binary devices, ternary OSCs show higher μ_e, indicating that the oligomer can also improve the electron transport ability in the device without TA treatment, which should firmly correlate with the morphology.

Trap-states often occur in the active layer, usually due to the non-optimized donor-acceptor phase distribution and low phase purity in the active layer. This trap-state can capture free carriers and become recombination centers, leading to a reduction in the J_{SC} and FF of the device.[45] Here, the electron-only devices were applied to investigate the effects of oligomer and TA treatment on the trap-state of control binary and ternary systems. The trap-state density (N_{trap}) can be evaluated by the equation:[45]

$$N_{\text{trap}} = \frac{2\varepsilon_0\varepsilon_r V_{\text{TFL}}}{qL^2}$$

where ε_0 is the permittivity of free space, ε_r is the relative permittivity of the material, V_{TFL} is the trap-filled limit voltage, q is the elementary charge, and L is the thickness of the active layer. As shown in Figure S7, for the control binary system, the trap-state density is calculated as 9.85×10^{15} cm^{-3} with TA treatment. After adding appropriate proportions of 5BDDBDT-F and 5BDDBDT-Cl, the electron trap-state densities of ternary devices are reduced to 9.08×10^{15} cm^{-3} and 8.55×10^{15} cm^{-3}, respectively. Moreover, without TA treatment, the trap-state density of oligomer-based ternary devices showed a significant reduction, from 9.78×10^{15} cm^{-3} of control device to 8.77×10^{15} cm^{-3} of 5BDDBDT-F-based ternary device and 8.05×10^{15} cm^{-3} 5BDDBDT-Cl-based device. The reduced trap state densities after the addition of oligomers would contribute to the enhanced J_{SC} and FF. These results indicate that non-TA treatment and oligomer coupling strategy are effective in repairing the morphological defects of the active layer.

To investigate the influence of oligomer on charge recombination in blend films, the *J-V* curves under different light intensity were measured, and the results are shown in **Figure 3b-c**. The relationship between light intensity (P_{light}) and J_{SC} can be expressed

as $J_{SC} \propto P_{light}^{\alpha}$. Here, the index α indicates the degree of bimolecular recombination. When $\alpha = 1$, representing the bimolecular recombination is completely suppressed.[46] As shown in **Figure 3b**, all the α values of control, PM6:5BDDBDT-F:BTP-BO4Cl and PM6:5BDDBDT-Cl:BTP-BO4Cl OSCs (both with and without TA) are close to 0.99, indicating the bimolecular recombination in all the blend films is suppressed. Furthermore, the charge recombination mechanisms can be evaluated by using the relationship between V_{OC} and P_{light}, which can be described as $V_{OC} \propto (nkT/q)\ln P_{light}$. Here, k is the Boltzmann constant, T is the absolute temperature and q is the elementary charge. The slope of nkT/q can be used to determine the degree of bimolecular or trap-assisted recombination.[47] The slopes of the control, PM6:5BDDBDT-F:BTP-BO4Cl and PM6:5BDDBDT-Cl:BTP-BO4Cl OSCs are 1.095kT/q, 1.075 kT/q and 1.101 kT/q with TA, 1.096kT/q, 1.074 kT/q and 1.087 kT/q without TA, respectively. This suggests that trap-assisted recombination is also small in the ternary blends. The above results indicate that the third component of oligomer 5BDDBDT-F and 5BDDBDT-Cl can effectively promote exciton dissociation and inhibit trap-assisted recombination, which is conducive to the improvement of FF and J_{SC} in ternary OSCs. This may be due to the optimization of the morphology in the active layer by oligomers, as will be discussed in later sections.

To gain deeper insights into the underlying reasons for the remarkably high FF observed in oligomer-based ternary devices, we employed transient absorption spectroscopy (TAS) to investigate the dynamics of photo-induced charge transfer and recombination within distinct blend films. Using an 800 nm pump light, we selectively excited the acceptor BTP-BO4Cl, resulting in the emergence of several bleach peaks within the 540-660 nm range. In Figure 3e-g), we present the 2D color plot for PM6:BTP-BO4Cl binary, 5BDDBDT-F, and 5BDDBDT-Cl ternary blend films, respectively, without TA treatment. These peaks closely align with the absorption features of the donors (as shown in Figure 1b and Figure S1b). Notably, since BTP-BO4Cl exhibited no TA signal within the 540-660 nm range (as depicted in Figure 1b

and Figure S1b), the appearance of peaks within this region indicates effective hole transfer at the interfaces between donors and acceptors. We closely monitored the rising kinetics of the ground-state bleach (GSB) of the donors at this wavelength (depicted in **Figure 3i-k**). The observed decay process for the photoexcited acceptor at 750 nm corresponds well with the rising GSB of the donors at 630 nm, showcasing the efficiency of hole transfer at these donor/acceptor interfaces. Quantitatively, the decay lifetimes of singlet excitons were determined as 1.96, 2.86, and 2.51 ps for PM6:BTP-BO4Cl binary, 5BDDBDT-F, and 5BDDBDT-Cl ternary blend films, respectively (refer to **Figure 3h**). It's crucial to note that while longer decay lifetimes might suggest slower processes, they don't necessarily imply a hindrance to charge generation; rather, they provide information about the intricate interplay of factors contributing to highly efficient charge generation in spite of the comparatively slower kinetics.[48] In addition to these findings, the V_{eff}-J_{ph} curves indicate that 5BDDBDT-F and 5BDDBDT-Cl-based ternary devices exhibit enhanced exciton dissociation. Moreover, according to the SCLC measurements, the hole and electron mobility of ternary devices involving 5BDDBDT-F and 5BDDBDT-Cl, without undergoing TA treatment, surpass those of the control. This implies that singlet excitons within the 5BDDBDT-F and 5BDDBDT-Cl-based ternary blend films are capable of traveling over longer distances, thus facilitating their reach to the donor-acceptor interface. This observation intriguingly suggests that the introduction of the oligomer component has a modifying effect on the host system's exciton diffusion properties. Furthermore, we investigated the lifetime of the polaron (as illustrated in **Figure 3l**), revealing that both ternary films exhibit slightly slower sub-nanosecond recombination of polarons. This signifies that the oligomer component has the potential to mitigate bimolecular recombination, thereby favorably contributing to improvements in FF.[48]

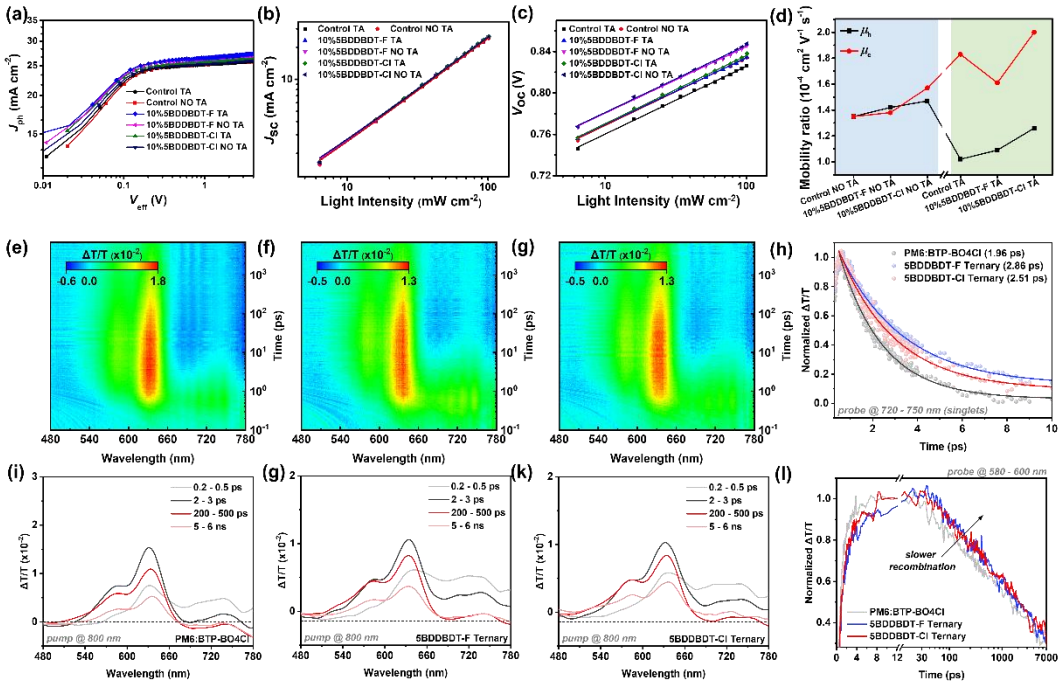

Figure 3. a) The curves of J_{ph} versus V_{eff} in the optimized solar cells. b) The dependence of P_{light} on J_{SC} of the solar cells. c) The dependence of P_{light} on V_{oc} of the solar cells. d) The μ_h and μ_e of the solar cells. e-g) 2D color plot of fs-TA spectra of control, 5BDDBDT-F and 5BDDBDT-Cl-based ternary blend at indicated delay times under 800 nm excitation with a fluence below 10 μJ cm^{-2}. h) Lifetime of single exciton with the corresponding sum of exponential fittings. i-k) Representative fs-TA spectra at indicated delay times. (l) Hole polaron generation and recombination dynamics with the corresponding sum of exponential fittings.

Morphology Characterization

The molecular stacking and orientation of the neat and blend films were investigated by the grazing-incidence wide angle X-ray scattering (GIWAXS) (**Figure 4** and Figure S8). 5BDDBDT-F neat film exhibits weak π-π staking and strong lamellar accumulation, which shows a lamellar diffraction peak (100) at 0.320 $Å^{-1}$ (d-spacing is 19.63 $Å^{-1}$) in the out-of-plane (OOP) with the crystal coherence lengths (CCLs) of 115.3 Å, according to the Scherrer equation: CCLs = $2\pi K/w$, where K is the Scherrer factor (K = 0.9) and w is the width at the half-maximum of the peak.[49] In contrast, 5BDDBDT-Cl neat film exhibits a weak (010) π-π stacking peak at 1.756 $Å^{-1}$ with a d-spacing of 3.58 Å in OOP direction, which dominates the face-on orientation relative to the substrate. Meanwhile, 5BDDBDT-Cl neat film shows a strong lamellar

accumulation, with a lamellar diffraction peak (100) at 0.322 $Å^{-1}$ (d-spacing is 19.50 $Å^{-1}$) in OOP direction, indicating that this type of oligomer is highly crystalline. We first check the molecular packing of the as-cast blend films. For the control blend film, the (100) diffraction peak in plane (IP) direction is located at 0.298 $Å^{-1}$ (d = 21.07 Å) and the (010) diffraction peak in the OOP direction is located at 1.742 $Å^{-1}$ (d = 3.61 Å), respectively. The (100) diffraction peaks in IP direction of the blend films based on PM6:5BDDBDT-F:BTP-BO4Cl and PM6:5BDDBDT-Cl:BTP-BO4Cl are located at 0.302 $Å^{-1}$ (d = 20.79 Å) and 0.311 $Å^{-1}$ (d = 20.19 Å). In addition, the (010) diffraction peaks in the OOP direction of PM6:5BDDBDT-F:BTP-BO4Cl and PM6:5BDDBDT-Cl:BTP-BO4Cl-based ternary blend films are located at 1.760 $Å^{-1}$ (d = 3.56 Å) and 1.767 $Å^{-1}$ (d = 3.55 Å). Based on the above results, it was found the introduction of 5BDDBDT-F or 5BDDBDT-Cl plays a key role in improving both the lamella and the π-π stacking. Moreover, the improved CCLs of (010) π-π stacking peaks in both ternary films (27.3 Å for 5BDDBDT-F-based and 28.4 Å for 5BDDBDT-Cl-based films versus 25.8 Å for control film) verifies that the doping of two oligomers would induce longer range of molecular ordering and thus positively regulate the crystallinity of active layer, which would benefit the transport properties. For the thermally annealed films, we found that the crystalline changes in a different way from as-cast to the TA procedure. The control film shows an improved crystallinity after the TA treatment, reflected by the prolonged CCL value of (010) π-π stacking from 25.8 to 27.8 Å. On the contrary, both the ternary films experienced a gradually decreased trend in (010) π-π stacking ordering from 27.3 Å to 26.4 Å for 5BDDBDT-F-based and from 28.4 Å to 22.7 Å for 5BDDBDT-Cl-based films. However, in the meantime, the lamellar crystallinity shows an increased trend with CCLs prolonging from 71.5 Å to 95.8 Å for 5BDDBDT-F-based and from 42.8 Å to 95.8 Å for 5BDDBDT-Cl-based films, respectively. Furthermore, as evident from Figure S8, the (100) peak positions of the BTP-BO4Cl neat film, BTP-BO4Cl:5BDDBDT-F, and BTP-BO4Cl:5BDDBDT-Cl blended films are all located at 0.398 $Å^{-1}$, corresponding to lamellar stacking distances of 15.8 Å. However, the CCL increases from 83.2 Å in the BTP-BO4Cl neat film to 84.3 Å in the BTP-BO4Cl:5BDDBDT-F film and 89.7 Å in the BTP-BO4Cl:5BDDBDT-Cl film. Moreover, the (010) peaks of the BTP-BO4Cl neat film, BTP-BO4Cl:5BDDBDT-F, and BTP-BO4Cl:5BDDBDT-Cl blended films are located at 1.81 $Å^{-1}$, 1.81 $Å^{-1}$, and 1.83 $Å^{-1}$, respectively, corresponding to π-π stacking distances of 3.47 Å, 3.47 Å, and 3.43 Å. The CCL also increases from 20.2 Å in the pure BTP-BO4Cl film to 20.9 Å in

the BTP-BO4Cl:5BDDBDT-F film and 22.6 Å in the BTP-BO4Cl:5BDDBDT-Cl film. Based on these, we can rationally deduce that adding oligomers can enlarge the processing windows (without TA or TA) in the way of improving the morphological structure by balancing the lateral crystallinity and π-π stacking along the vertical direction relative to the substrate.

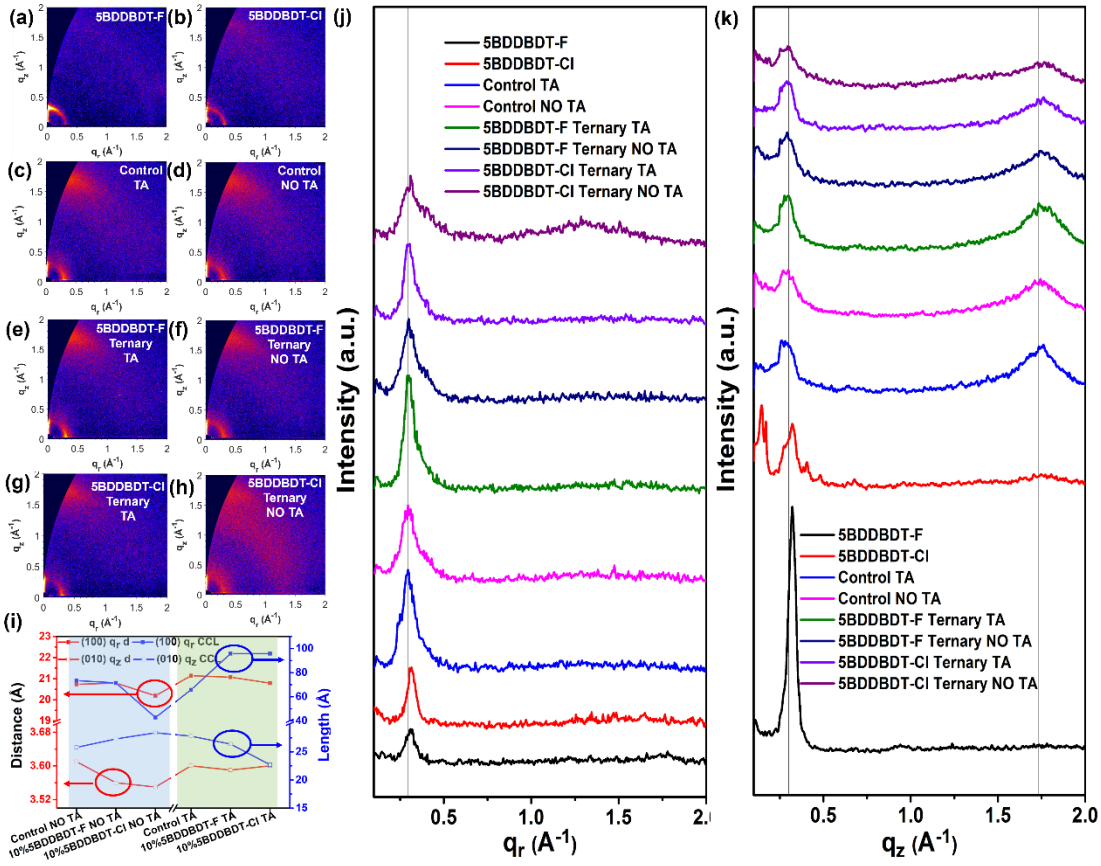

Figure 4. 2D GIWAXS patterns of a-b) neat films and c-h) blend films under optimal conditions. i) The curves of lamellar and π-π stacking distance, and CCLs of π-π stacking. The 1D line cuts along j) in-plane and k) out-of-plane of the corresponding films.

To get deeper insights of the way how the oligomers affect the film crystallinity, we probed the film formation kinetics of the optimal binary and ternary films from spin coating process to post-treatment process using in situ UV–vis reflection measurement, as shown in **Figure 5**. The raw reflection line cuts are provided in Figure S9, from which the time-resolved absorbance information could be extracted and analyzed. The distinct absorption profiles of the donor and acceptor enable the analysis of their respective crystallization behaviors. The peak intensity and location evolution of the

corresponding films varying with spin coating time are displayed in **Figure 5**a-c. The whole spin coating processes can be divided into four stages. Stage I and II: The intensity of donor and acceptor increases at two varied increasing rates, among which the former rapid rate attributes to the fast evaporation of solvent (Stage I) and the slower rate is typically defined as the pre-aggregation process (liquid-liquid transition) (Stage II).[10] Stage III: The position of both the donor and acceptor begins to red shift and peak intensity rapid increased, indicating phase transition from solution to solid occurs, i.e. aggregation process of materials. Here, the pre-aggregation and aggregation rates are derived from the slopes, and the time required for the corresponding stages are shown in **Figure 5d-f** for better comparison. Stage IV: The locations and intensity remain constant for all the materials.

Compared to the binary film at the wetting stage, the intensity of both ternary films' upturns at faster rates (Donor: 0.19, 0.47, 0.83 s^{-1}; Acceptor: 0.52, 0.66, 0.74 s^{-1}) and with similar time, indicating that introduction of oligomers could facilitate the pre-aggregation kinetics of both host donor and acceptor in the liquid state. Subsequently, the aggregation period (Stage III) occurs with the solution concentration further increased. It was found that aggregation rates of these three blend films are 1.69, 2.54, 2.78 s^{-1} for PM6 and 4.79, 6.6, 8.06 s^{-1} for BTP-BO4Cl, respectively (**Figure 5d-f**). This finding indicates that oligomers can significantly accelerates the PM6 and BTP-BO4Cl phase separational pre-aggregation and aggregation procedures in spin coating. In order to verify whether this effect is also effective in the blade-coating device, we investigated the in-situ UV characteristics of control binary, 5BDDBDT-F, and 5BDDBDT-Cl-based ternary blend films in blade-coating process, as shown in Figures S10, S11, S12, and S13. When with TA treatment, the process of change in the positions of the maximum absorption peaks for both PM6 and BTP-BO4Cl revealed that the pre-aggregation rates for PM6 in the control binary, 5BDDBDT-F, and 5BDDBDT-Cl-based ternary blend films are 1.04, 1.45, and 1.08 s^{-1}, respectively, while the aggregation rates are 6.96, 11.11, and 7.69 s^{-1}. For BTP-BO4Cl, the pre-aggregation rates are 0.89, 1.1, and 1.09 s^{-1}, respectively, and the aggregation rates are 25.92, 27.53, and 49.17 s^{-1}.

Additionally, by examining the changes in the intensity of the maximum absorption peaks for both PM6 and BTP-BO4Cl, we observed that the pre-aggregation rates for PM6 in the control binary, 5BDDBDT-F, and 5BDDBDT-Cl-based ternary blend films are 0.036, 0.031, and 0.093, respectively, while the aggregation rates are 0.68, 2.18, and 1.01. For BTP-BO4Cl, the pre-aggregation rates are 0.70, 0.80, and 1.04, and the aggregation rates are 1.27, 1.69, and 1.87. Furthermore, when no thermal annealing is performed, the phenomena are similar to those observed during annealing. Whether based on the changes in the maximum absorption peaks of the donor and acceptor or the corresponding intensity variations, the calculated pre-aggregation and aggregation rates of the donor-acceptor pairs are consistently higher in the ternary blend films (as shown in Figure S13). These results suggest that the oligomer component can also facilitate the pre-aggregation and aggregation of the host material during the blade-coating process. This is the reason why the FF and PCE of small area ternary blade-coated devices are higher compared to those of control blade-coated devices. Compared with spin-coated devices, the drying time of the active layer film is longer during the preparation of the blade-coated devices, which provides a longer time for the aggregation of the active layer material and the formation of a tighter, more regular aggregation, which is beneficial for the improvement of FF. Based on above results, we speculate that a small content of oligomers typically featuring high crystalline properties provide the nuclei seeding sites for the host materials' crystalline growth, thereby promoting the pre-aggregation and aggregation of donor and acceptor, which is favorable to get high quality crystallites and thus charge transport. Subsequently, in situ reflection measurements performed on three thermally annealed (100 ^{o}C) films are also summarized in Figure S9. We found that the reflection intensity of the three films all changed with prolonged TA time, while no obvious BTP-BO4Cl peak location change with only 1 nm shift, which may come from the measurement error (shown in Figure S9). Herein, the intensity changes only elucidate the removal of the remaining solvents in the films with no obviously additional phase transitions.

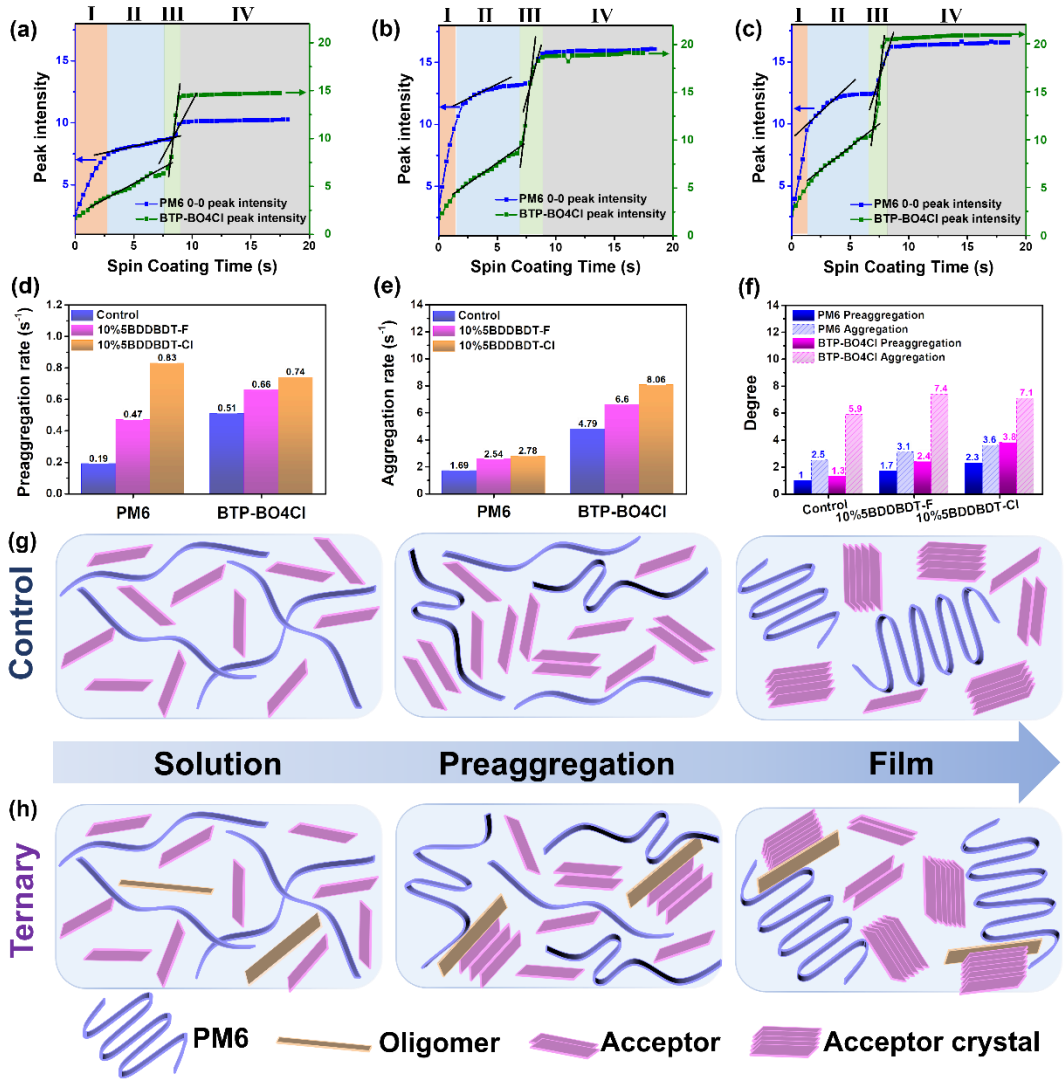

Figure 5. Time-dependent PM6 0–0 peak, BTP-BO4Cl peak and peak intensity evolution monitored by in situ UV-vis absorption spectra during spin coating processes: a) control, b) 10%5BDDBDT-F, c) 10%5BDDBDT-Cl. d) Pre-aggregation rates and e) Aggregation rates of donor and acceptor of the corresponding films during spin coating processes. f) The degree of pre-aggregation and aggregation rates in the corresponding films during spin coating processes. g, h) Schematic diagram of molecular aggregation state of control and ternary active layer during spin coating.

To analyze the effect of oligomers on morphology, the tapping-mode atomic force spectroscopy (AFM) was used to study the surface morphologies of the blend films, AFM height images were shown in Figure S14. The blend films of control, PM6:5BDDBDT-F:BTP-BO4Cl and PM6:5BDDBDT-Cl:BTP-BO4Cl exhibit the similar root-mean-square (RMS) roughness (1.05, 1.14, and 1.01 nm) after the TA treatment. Surprisingly, the RMS values (1.61, 1.75, and 1.83 nm) of these three blend

films without the TA treatment increased significantly. In addition, the control, 5BDDBDT-F- and 5BDDBDT-Cl-based blend films showed similar RMS values after TA treatment, which may be due to the strong driving force of external heating that would inhibit the ability of oligomer-induced aggregation.[44,50] In contrast, under mild conditions without TA treatment, the oligomer-induced aggregation ability can be fully demonstrated with faster pre-aggregation and aggregation rates and similar time to form larger phase separation patterns of donor and acceptor. Thus, the oligomer-based blend films exhibited larger RMS values relative to control without TA treatment, which is consist with the result of in situ UV-vis.

The phase separation of the active layer is also driven by the thermodynamic miscibility of the donor and acceptor, which can be evaluated by the surface energy parameter. Here, contact angle measurements were used to define the surface energy of each component to further understand the reason for the difference in the active layer morphological evolution. As shown in Figure S15, the water contact angles of 5BDDBDT-F, 5BDDBDT-Cl, PM6 and BTP-BO4Cl were 97.97°, 99.60°, 102.08° and 92.55°, respectively. The ethylene glycol (EG) contact angle were measured as 70.22°, 70.65°, 71.75° and 64.42°, respectively. Thus, their surface energies are calculated as 27.31, 28.72, 30.46 and 29.03 mN m^{-1}, (Table S5, supporting information) respectively, according to empirical formulas.[51] The compatibility of two different compounds can be estimated by the following equation:

$$\gamma_{A\text{-}B} = \gamma_A + \gamma_B - 4\left(\frac{\gamma_A^d \gamma_B^d}{\gamma_A^d + \gamma_B^d} + \frac{\gamma_A^p \gamma_B^p}{\gamma_A^p + \gamma_B^p}\right)$$

Here, $\gamma_{A\text{-}B}$ is defined as the interfacial tension between the compound A and B. γ_A and γ_B represent the surface energies of compounds A and B, respectively. γ^d and γ^p are the components of surface energy in the dispersive force and polar force, respectively. The calculated results are summarized in Table S5. It was found that the interfacial tension of $\gamma_{5BDDBDT\text{-}F\text{-}BTP\text{-}BO4Cl}$ (0.38 mN m^{-1}) and $\gamma_{5BDDBDT\text{-}Cl\text{-}BTP\text{-}BO4Cl}$ (0.93 mN m^{-1}) are both considerably smaller than $\gamma_{PM6\text{-}BTP\text{-}BO4Cl}$ (1.91 mN m^{-1}), indicating oligomer donors and BTP-BO4Cl acceptor had better compatibility than PM6.[36] In order to further investigate the position of the third component in the ternary system, the concept of wetting coefficient (ω) of the third component oligomer is introduced, which is

calculated according to Young's equation:[52]

$$\omega_{D_2} = \frac{\gamma_{D_1/D_2} - \gamma_{D_2/A}}{\gamma_{D_1/A}} \quad (2)$$

Here, γ_{D_1/D_2} refers to the interfacial tension between PM6 and the oligomer, and the meaning of $\gamma_{D_2/A}$ and $\gamma_{D_1/A}$ can be deduced by analogy, and these can be calculated by using Equation (1). When the wetting coefficient is greater than 1 ($\omega_{D_2} > 1$), component D_2 is located in the phase of component A (acceptor), while if $\omega_{D_2} < -1$, component D_2 is located in the domain of component D_1 (PM6). If $-1 < \omega_{D_2} < 1$, component D_2 will be located at the interface of D_1 and A.[53] As shown in Table S5, the $\omega_{5BDDBDT-F}$and $\omega_{5BDDBDT-Cl}$ are calculated as 0.495 and -0.573, respectively, indicating that oligomer 5BDDBDT-F and 5BDDBDT-Cl tend to be located at the interfaces between PM6 and BTP-BO4Cl. Noticeably, the compatibility results imply that the oligomers tend to diffuse to the acceptor domains, but we need to bear in mind that both thermodynamic and kinetic factors strongly affect the active layer phase separation. In real cases, many factors, like molecular interactions and film formation kinetics that competitively determine the location of third component and thus the final morphology.[54] To be specific, the better miscibility between oligomer and acceptor facilitates the oligomer to approach the acceptor, while the faster crystallization of both donor and acceptor induced by the highly crystalline oligomer, finally the combined effects make the oligomers vitrified from the acceptor domains and tend to move to the interfaces between the donor and acceptors phases. The aforementioned morphological results make our morphological pattern more visual: a small amount of oligomer more readily comes out as seeding sites to promote the pre-aggregation process in the liquid state, and subsequently accelerates the self-organization process in a prolonged period. And then oligomers tend to reassemble at the interfaces between PM6 and BTP-BO4Cl, and to facilitate more crystalline domains with enhanced molecular packings.[55] The corresponding morphological evolutions are illustrated in **Figure 5**g. In such a way, the oligomer can act as a bridging linker to rehabilitate the interfacial defects to reduce the trap-assisted recombination losses and thus to promote exciton dissociation and charge transport, and hence resulting in much higher FF and J_{SC} of the device.

Energy loss analysis

To better understand the underlying mechanism behind the abnormal increase of V_{OC} when the oligomers 5BDDBDT-F or 5BDDBDT-Cl with higher HOMO level were

introduced as the third component, we investigated the detailed energy losses (E_{loss}) of the control and the ternary devices. The E_{loss} in OSCs can be attributed to three terms,[56,57] as shown as follows:

$$q\Delta V = E_{gap} - qV_{OC}$$

$$= (E_{gap} - qV_{OC}^{SQ}) + (qV_{OC}^{SQ} - qV_{OC}^{rad}) + (qV_{OC}^{rad} - qV_{OC})$$

$$= (E_{gap} - qV_{OC}^{SQ}) + qV_{OC}^{rad,below\ gap} + qV_{OC}^{non-rad}$$

$$= \Delta E_1 + \Delta E_2 + \Delta E_3$$

Where E_{gap} is bandgap of the blend film, V_{OC}^{SQ} is the maximum voltage based on the Shockley–Queisser limit, V_{OC}^{rad} is the voltage when there is only radiative recombination, $V_{OC}^{rad,below\ gap}$ is the voltage loss of radiative recombination from the absorption below the bandgap, $V_{OC}^{non-rad}$ is the voltage loss originating from non-radiative recombination. The first term $\Delta E_1 = (E_{gap} - qV_{OC}^{SQ})$ is the radiative recombination loss originating from the absorption above the bandgap, which is inevitable for any type of solar cell, typically in the range of 0.25-0.30 eV.[58] The second term, $\Delta E_2 = (qV_{OC}^{rad,below\ gap})$, represents additional radiative recombination from the absorption below the bandgap, which can be evaluated by Fourier transform photocurrent spectroscopy (FTPS), as shown in **Figure 6**. The third term ($qV_{OC}^{non-rad} = -kT \ln EQE_{EL}$), the non-radiative recombination loss,[59] could be evaluated by external electroluminescence quantum efficiency (EQE_{EL}) of the solar cells, which is the dominant V_{OC} loss for OSCs with the values typically lying between 0.30-0.48 eV[60] Thus, reducing ΔE_3 is the key to reducing energy loss and increasing V_{OC} in non-fullerene systems. The values of E_{gap} of all devices were derived from the derivative of EQE_{PV} spectral edge (dEQE/dE), ΔE_2 and ΔE_3 were calculated by FTPS and EQE_{EL}, respectively, as shown in **Table 4 and Figure 6.** The E_{gap}s of PM6:BTP-BO4Cl-based binary devices, 10%5BDDBDT-F and 10%5BDDBDT-Cl-based ternary devices are 1.39 eV, 1.38 eV, 1.38 eV with TA, and all 1.39 eV without TA, respectively. After the TA treatment, ternary blend film shows a reduced E_{gap}, due to the red-shift of the absorption spectrum, which can be observed in the EQE curves. As shown in **Table 4**,

all devices show similar ΔE_1 values (0.26 eV) and negligible ΔE_2 (in the range of 0.05-0.06 eV). With the addition of oligomers, the values of ΔE_3 are reduced for both as-cast and thermally annealed devices, resulting from the increased EQE_{EL} of the oligomer-based devices. The energetic disorder of OSCs can be evaluated by Urbach energy (Eu) by fitting FTPS-EQE- absorption edge in lower energy region, according to the equation as follows: $\alpha(E) = \alpha_0 e^{\frac{E-E_g}{E_U}}$. The lower Eu means lower energetic order and thus negligible trap states. The Eu values of binary devices are suppressed after doping the oligomers, contributing to the lower radiative and nonradiative recombination losses. Ultimately, the PM6:BTP-BO4Cl-based binary device shows a higher E_{loss}s of 0.56 eV with TA, and 0.55 eV without TA. When introducing oligomers 5BDDBDT-F or 5BDDBDT-Cl, the E_{loss}s of ternary devices decreased to 0.54, 0.55 eV with TA, and 0.53, 0.54 eV without TA, which is consistent with the increase of V_{OC} in the ternary solar cells. Thereby, the lower energy losses are closely associated with the decreased energetic disorder and trap states, which benefits from the optimized morphology as discusses above, rather than the typically energy levels-dominant V_{OC} increment mechanisms claimed by previous ternary works.[61,62]

Table 4. Summary of energy loss parameters of binary and ternary devices based on PM6:oligomer:BTP-BO4Cl system measured and calculated from FTPS-EQE and EL.

Device	E_g[a] (eV)	V_{OC} (V)	ΔE (eV)	$V_{OC,SQ}$ (V)	$V_{OC,rad}$ (V)	EQE_{EL} (%)	ΔE_1 (eV)	ΔE_2 (eV)	ΔE_3 (eV)	Eu (meV)
Control TA	1.39	0.834	0.56	1.13	1.07	9.08×10^{-3}	0.26	0.06	0.239	28.2
Control NO TA	1.39	0.840	0.55	1.13	1.07	1.25×10^{-2}	0.26	0.06	0.231	27.1
10%5BDDBDT-F TA	1.38	0.840	0.54	1.12	1.07	1.57×10^{-2}	0.26	0.05	0.224	26.5
10%5BDDBDT-F NO TA	1.39	0.846	0.53	1.13	1.06	1.70×10^{-2}	0.26	0.05	0.222	26.4
10%5BDDBDT-Cl TA	1.38	0.846	0.55	1.12	1.08	1.55×10^{-2}	0.26	0.06	0.225	27.0
10%5BDDBDT-Cl NO TA	1.39	0.857	0.54	1.13	1.07	1.83×10^{-2}	0.26	0.06	0.220	26.7

[a]E_g was obtained from the derivatives of the EQE_{PV} spectra.

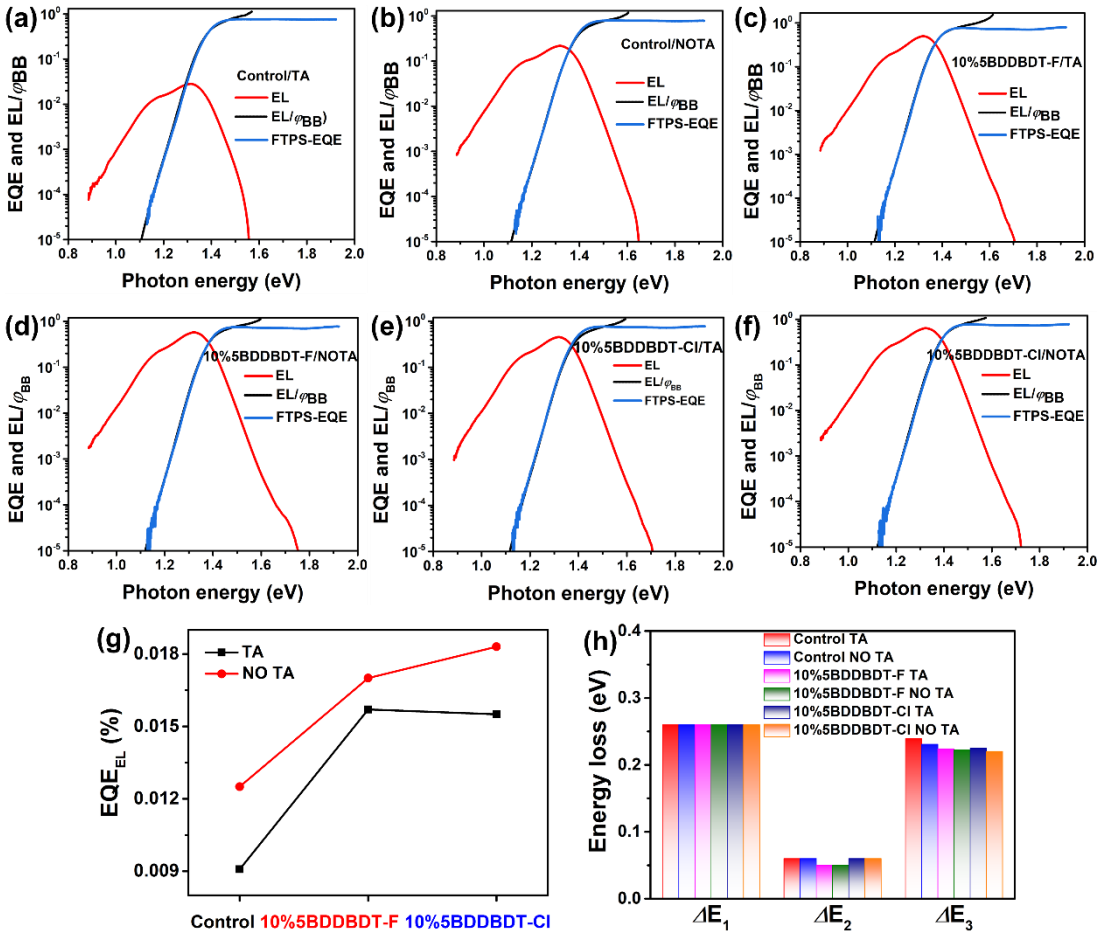

Figure 6. The normalized FTPS-EQE and EL spectra of different OSCs (a-f). The comparison of EQE_{EL} (g), ΔE_1, ΔE_2 and ΔE_3 values (h) of different OSCs.

Stability, universality and scalability

The stability of OSCs is key toward commercial applications, which is closely related to the stability of the active layer morphology. Thus, we investigated the room-temperature thermal stability and optical stability of these OSCs. Figure S16 shows the corresponding evolution for normalized PCEs over time. The unencapsulated devices were heated at 80°C in a nitrogen-filled glove box to study their thermal stability. After 450 hours, the performance of the control devices with and without thermal annealing was 63.4% and 55.0% of the initial performance. However, the performance of the three components based on 5BDTBDD-F and 5BDDBDT-Cl maintained 67.8% and 66.2%, 69.5% and 67.0% of the initial values, respectively. To further investigate the optical stability of these devices, the encapsulated devices were placed in the air under sunlight exposure. After 450 h, the performance of the thermal annealing and non-thermal

annealing control devices maintained only 90.5% and 89.9% of the initial performance, respectively. However, the performance of the ternary devices based on 5BDDBDT-F and 5BDDBDT-Cl with or without thermal annealing maintained 91.5% and 93.6% (5BDDBDT-F-based), 92.0% and 93.9% (5BDDBDT-Cl-based) of the initial values, respectively. This indicates that the stability performance of oligomer-based ternary devices is significantly better than the binary control devices in terms of storage stability at room temperature and thermal stability. It is noteworthy that the control devices exhibit significant burn-in losses due to due to the unstable molecular configuration and active layer morphology. However, when introducing the oligomer into the PM6:BTP-BO4Cl host blend, the oligomers act as a bridge between the polymer donor and the small molecule acceptor, facilitating the aggregation of the donor and acceptor while immobilizing the donor and acceptor phases, thereby significantly inhibiting the burn-in losses degradation of the ternary devices.

We investigated the universality of this oligomerization strategy on another well-known system PM6:BTP-eC9.[63] The chemical structures of the BTP-eC9, *J-V* and EQE curves for PM6:oligomer:BTP-eC9 are shown in **Figure 1a, 2d** and **2e**, respectively, and the relevant data are summarized in **Table 4**. For the PM6:oligomer:BTP-eC9 system, all devices were fabricated under the same optimal processing condition as for the PM6:oligomer:BTP-BO4Cl system. With a TA treatment of 100ºC for 10 min, PM6:5BDDBDT-F:BTP-eC9-based and PM6:5BDDBDT-Cl:BTP-eC9-based ternary devices obtain outstanding PCEs of 18.28% with a V_{OC} of 0.839 V, a FF of 79.0%, and 18.21% with a V_{OC} of 0.841 V, a FF of 79.12%, respectively, which are obvious higher than the PM6:BTP-eC9-based devices of 17.50%. It is important to note that the PM6:5BDDBDT-F:BTP-eC9-based and PM6:5BDDBDT-Cl:BTP-eC9-based ternary devices yield a superior PCE of 18.32% with a V_{OC} of 0.850 V, a FF of 79.15%, and a PCE of 18.43% with a V_{OC} of 0.854 V, a FF of 79.29%, respectively, representing the state-of-the-art of annealing free OSCs.

Encouraged by the achieved superior morphology and the intrinsic printing friendly advantages of green-solvent processing and thermal-annealing-insensitivity, we baldly

transfer the glovebox spin coating (4.2 mm^2 device) to open air blade coating (1cm^2) to test the manufacturability.[31,64,65] The ternary devices based on PM6:BTP-eC9 with 1 cm^2 areas obtained outstanding PCEs of 17.11% (with 5BDDBDT-F) and 17.06% (with 5BDDBDT-Cl), decent FFs of 73.09% and 73.08% (**Figure 2e**), respectively, which are one of the highest values of PCE and FF for the large-area green-solvent processed blade coating OSCs (**Figure 2i**). It's worth noting that these PCE values have been independently certified at 17.22% and 17.37% (as shown in Figure S17 and Table S6). It demonstrated that those devices with an excellent FF using green solvent *o*-xylene without any posttreatments exhibit their great potential for the device upscaling.

3. Conclusion

In summary, we demonstrated that the strategy of novel oligomers assists to control crystallization kinetics is targeted to tailor the two-phase transitions of active layer: liquid-to-liquid, and liquid to solid transitions. We uncovered the film morphological and device physical mechanisms underlying the strategy, including the enhanced crystallinity, the reduced interfacial defects and the inhibited nonradiative recombination losses. Furthermore, we emphasize the morphological landscape effects on the energetic losses rather than the energy level-dominant V_{OC} increase mechanisms. Benefiting from the superior morphology tuning and energy loss suppression, a series of high-efficiency, green-solvent processed and annealing-free OSCs were achieved with PCEs of 18.32% and 18.43% for 4.2 mm^2 devices and 17.11% and 17.06% for 1cm^2 large area devices. This work provided a new insight of the correlations among morphology formation kinetics, device physics and device performance, which offers guidance on the effective optimization of OSC devices pacing pathway towards coming industrial production.

Author contributions

H. Xia and Y. Zhang conceived the idea, designed the experiments and prepared the manuscript. K. Liu provided AFM images and analysis. W. Deng performed energy loss measurements and analysis. M. Zhu and H. Tan provided the raw materials for the synthesis. P. Fong performed in-situ UV-vis. H. Liu, X. Xia and X. Lu provided the GIWAXS measurements. T. A. D. Peña, R. Ma, M. Li and J. Wu provided the TAS

measurements. M. Zhang and W. Wong provided the MALDI-TOF measurements. Y. Lang helped fabricate and optimize the blade coating devices. J. Fu helped in the study of device data. W. Zhu and G. Li supervised the project and contributed to the revision of the manuscript.

Acknowledgement

Thanks to the financial supports from the National Natural Science Foundation of China (22275024, 51673031), the Research Innovation Program for Postgraduate of Jiangsu Province (KYCX22_3032, KYCX21_2776, SJCX21_1247), the Top-notch Academic Programs Project of Jiangsu Higher Education Institutions (TAPP) and The Priority Academic Program Development of Jiangsu Higher Education Institutions (PAPD), Jiangsu Provincial Talents Project of High-Level Innovation and Entrepreneurship, the Research Grants Council of Hong Kong (GRF 152221320, CRF C5037-18G, SRFS2223-5S01), the Shenzhen Science and Technology Innovation Commission (JCYJ 20200109105003940), the Hong Kong Polytechnic University (Sir Sze-yuen Chung Endowed Professorship Fund (8-8480), G-SAC5), and Guangdong-Hong Kong-Macao Joint Laboratory for Photonic-Thermal-Electrical Energy Materials and Devices (GDSTC No. 2019B121205001). Finally, thanks to the Prof. Alex Jen and Dr. Baobing Fan of the City University of Hong Kong for their support of the device efficiency certification.

Supporting Information

Details of characterization, measurement, and synthetic methods; ^{1}H, ^{13}C NMR spectra and Time-of-Flight (MALDI-TOF) analyzer data; UV, DFT, J-V, PL, SCLC, GIWAXS, In Situ UV, AFM, Contact Angle, Stability measurement data.

References

[1] G. Yu, J. Gao, J. C. Hummelen, F. Wudi, A. J. Heeger, *Science* **1995**, *270*, 1789.

[2] Y. Cheng, S. Yang, C. Hsu, *Chem. Rev.* **2009,** *109*, 5868.

[3] G. Li, R. Zhu, Y. Yang, *Nat. Photon.* **2012,** *6*, 153.

[4] L. Dou, Y. Liu, Z. Hong, G. Li, Y. Yang, *Chem. Rev.* **2015,** *115*, 12633. 44.

[5] Y. Cui, Y. Xu, H. Yao, P. Bi, L. Hong, J. Zhang, Y. Zu, T. Zhang, J. Qin, J. Ren, Z. Chen, C. He, X. Hao, Z. Wei, J. Hou, *Advanced Materials* **2021,** *33*, 2102420.

[6] L. Zhu, M. Zhang, J. Xu, C. Li, J. Yan, G. Zhou, W. Zhong, T. Hao, J. Song, X. Xue, Z. Zhou, R. Zeng, H. Zhu, C.-C. Chen, R. C. I. MacKenzie, Y. Zou, J. Nelson, Y. Zhang, Y. Sun, F. Liu, *Nature Materials* **2022**.

[7] K. Chong, X. Xu, H. Meng, J. Xue, L. Yu, W. Ma, Q. Peng, *Advanced Materials* **2022,** *34*, 2109516.

[8] W. Gao, F. Qi, Z. Peng, F. R. Lin, K. Jiang, C. Zhong, W. Kaminsky, Z. Guan, C. S. Lee, T. J. Marks, H. Ade, A. K. Y. Jen, *Advanced Materials* **2022,** *34*, 2202089.

[9] Y. Wei, Z. Chen, G. Lu, N. Yu, C. Li, J. Gao, X. Gu, X. Hao, G. Lu, Z. Tang, J. Zhang, Z. Wei, X. Zhang, H. Huang, *Advanced Materials* **2022,** *34*, 2204718.

[10] X. Song, Y. Song, H. Xu, S. Gao, Y. Wang, J. Li, J. Hai, W. Liu, W. Zhu, *Advanced Energy Materials* **2022,** *13*, 2203009.

[11] J. Yuan, Y. Zhang, L. Zhou, G. Zhang, H.-L. Yip, T.-K. Lau, X. Lu, C. Zhu, H. Peng, P. A. Johnson, M. Leclerc, Y. Cao, J. Ulanski, Y. Li, Y. Zou, *Joule* **2019,** *3*, 1140-1151.

[12] H. Tang, T. Xu, C. Yan, J. Gao, H. Yin, J. Lv, R. Singh, M. Kumar, T. Duan, Z. Kan, S. Lu, G. Li, *Advanced Science* **2019,** *6*, 1901613.

[13] G. Li, C. W. Chu, V. Shrotriya, J. Huang, Y. Yang, *Applied Physics Letters* **2006,** *88*, 253503.

[14] Y. Zhang, K. Liu, J. Huang, X. Xia, J. Cao, G. Zhao, P. W. K. Fong, Y. Zhu, F. Yan, Y. Yang, X. Lu, G. Li, *Nature Communications* **2021,** *12*. 4815.

[15] B. Qiu, Z. Chen, S. Qin, J. Yao, W. Huang, L. Meng, H. Zhu, Y. Yang, Z. G. Zhang, Y. Li, *Advanced Materials* **2020,** *32*, 1908373.

[16] G. Li, V. Shrotriya, J. Huang, Y. Yao, T. Moriarty, K. Emery, Y. Yang, Nature Materails **2005**, 4, 864-868.

[17] Z. Wang, Z. Peng, Z. Xiao, D. Seyitliyev, K. Gundogdu, L. Ding, H. Ade, *Advanced Materials* **2020,** *32*, 2005386.

[18] R. Sun, Y. Wu, J. Guo, Y. Wang, F. Qin, B. Shen, D. Li, T. Wang, Y. Li, Y. Zhou, G. Lu, Y. Li, J. Min, *Energy & Environmental Science* **2021,** *14*, 3174-3183.

[19] D. Hu, Q. Yang, H. Chen, F. Wobben, V. M. Le Corre, R. Singh, T. Liu, R. Ma, H. Tang, L. J. A. Koster, T. Duan, H. Yan, Z. Kan, Z. Xiao, S. Lu, *Energy & Environmental Science* **2020,** *13*, 2134-2141.

[20] H. Chen, D. Hu, Q. Yang, J. Gao, J. Fu, K. Yang, H. He, S. Chen, Z. Kan, T. Duan, C. Yang, J. Ouyang, Z. Xiao, K. Sun, S. Lu, *Joule* **2019,** *3*, 3034-3047.

[21] S. Dong, T. Jia, K. Zhang, J. Jing, F. Huang, *Joule* **2020,** *4*, 2004-2016.

[22] Z. Abbas, S. U. Ryu, M. Haris, C. E. Song, H. K. Lee, S. K. Lee, W. S. Shin, T. Park, J.-C. Lee, *Nano Energy* **2022,** *101*, 107574.

[23] X. Song, P. Sun, D. Sun, Y. Xu, Y. Liu, W. Zhu, *Nano Energy* **2022,** *91*, 106678.

[24] R. Sun, T. Wang, Y. Wu, M. Zhang, Y. Ma, Z. Xiao, G. Lu, L. Ding, Q. Zheng, C. J. Brabec, Y. Li, J. Min, *Advanced Functional Materials* **2021,** *31*, 2106846.

[25] J. Liu, J. Deng, Y. Zhu, X. Geng, L. Zhang, S. Y. Jeong, D. Zhou, H. Y. Woo, D. Chen, F. Wu, L. Chen, *Advanced Materials* **2022,** *35*, 2208008.

[26] L. Lu, M. A. Kelly, W. You, L. Yu, *Nature Photonics* **2015,** *9*, 491-500.

[27] P. Bi, X. Hao, *Solar RRL* **2019,** *3*, 1800263.

[28] R. Yu, H. Yao, J. Hou, *Advanced Energy Materials* **2018,** *8*, 1702814.

[29] Y. Zhang, G. Li, *Accounts of Materials Research* **2020,** *1*, 158-171.

[30] N. Gasparini, A. Salleo, I. McCulloch, D. Baran, *Nature Reviews Materials* **2019,** *4*, 229-242.

[31] Y. Liu, J. Zhao, Z. Li, C. Mu, W. Ma, H. Hu, K. Jiang, H. Lin, H. Ade, H. Yan, *Nature Communication* **2014,** *5*, 5293.

[32] Y. Wang, X. Wang, B. Lin, Z. Bi, X. Zhou, H. B. Naveed, K. Zhou, H. Yan, Z. Tang, W. Ma, *Advanced Energy Materials* **2020,** *10*, 2000826.

[33] H. Zhao, H. B. Naveed, B. Lin, X. Zhou, J. Yuan, K. Zhou, H. Wu, R. Guo, M. A. Scheel, A. Chumakov, S. V. Roth, Z. Tang, P. Müller‐Buschbaum, W. Ma, *Advanced Materials* **2020,** *32*, 2002302.

[34] B. Lin, X. Zhou, H. Zhao, J. Yuan, K. Zhou, K. Chen, H. Wu, R. Guo, M. A. Scheel, A. Chumakov, S. V. Roth, Y. Mao, L. Wang, Z. Tang, P. Müller-Buschbaum, W. Ma, *Energy & Environmental Science* **2020,** *13*, 2467-2479.

[35] P. Bi, S. Zhang, T. Xiao, M. Cui, Z. Chen, J. Ren, C. Qin, G. Lu, X. Hao, J. Hou, *Science China Chemistry* **2021,** *64*, 599-607.

[36] H. Xia, Y. Zhang, W. Deng, K. Liu, X. Xia, C. J. Su, U. S. Jeng, M. Zhang, J. Huang, J. Huang, C. Yan, W. Y. Wong, X. Lu, W. Zhu, G. Li, *Advanced Materials* **2022,** *34*, 2107659.

[37] H. Xia, X. Xu, C. Qian, J. Guo, J. Zhao, K. Zhang, H. Tan, Q. Peng, W. Zhu, *ACS Applied Energy Materials* **2022,** *5*, 3146-3155.

[38] Z. Wang, X. Zhu, J. Zhang, K. Lu, J. Fang, Y. Zhang, Z. Wang, L. Zhu, W. Ma, Z. Shuai, Z. Wei, *Journal of the American Chemical Society* **2018,** *140*, 1549-1556.

[39] S. Li, L. Zhan, C. Sun, H. Zhu, G. Zhou, W. Yang, M. Shi, C.-Z. Li, J. Hou, Y. Li, H. Chen, *Journal of the American Chemical Society* **2019,** *141*, 3073-3082.

[40] Y. Cui, H. Yao, L. Hong, T. Zhang, Y. Tang, B. Lin, K. Xian, B. Gao, C. An, P. Bi, W. Ma, J. Hou, *National Science Review* **2020,** *7*, 1239-1246.

[41] P. W. M. Blom, V. D. Mihailetchi, L. J. A. Koster, D. E. Markov, *Advanced Materials* **2007,** *19*, 1551-1566.

[42] Y. Chen, R. Ma, T. Liu, Y. Xiao, H. K. Kim, J. Zhang, C. Ma, H. Sun, F. Bai, X. Guo, K. S. Wong, X. Lu, H. Yan, *Advanced Energy Materials* **2021,** *11*, 2003777.

[43] N. Yi, Q. Ai, W. Zhou, L. Huang, L. Zhang, Z. Xing, X. Li, J. Zeng, Y. Chen, *Chemistry of Materials* **2019,** *31*, 10211-10224.

[44] W. Zhu, A. P. Spencer, S. Mukherjee, J. M. Alzola, V. K. Sangwan, S. H. Amsterdam, S. M. Swick, L. O. Jones, M. C. Heiber, A. A. Herzing, G. Li, C. L. Stern, D. M. DeLongchamp, K. L. Kohlstedt, M. C. Hersam, G. C. Schatz, M. R. Wasielewski, L. X. Chen, A. Facchetti, T. J. Marks, *Journal of the American Chemical Society* **2020,** *142*, 14532-14547.

[45] Y. Zhang, G. Cai, Y. Li, Z. Zhang, T. Li, X. Zuo, X. Lu, Y. Lin, *Advanced Materials* **2021,** *33*, 2008134.

[46] L. Nian, K. Gao, Y. Jiang, Q. Rong, X. Hu, D. Yuan, F. Liu, X. Peng, T. P. Russell, G. Zhou, *Advanced Materials* **2017,** *29*, 1700616.

[47] L. J. A. Koster, V. D. Mihailetchi, R. Ramaker, P. W. M. Blom, *Applied Physics Letters* **2005,** *86*, 123509.

[48] T. A. D. Peña, R. Ma, Z. Xing, Q. Wei, J. I. Khan, R. M. Young, Y. Hai, S. A. Garcia, X. Zou, Z. Jin, F. L. Ng, K. L. Yeung, D. F. Swearer, M. R. Wasielewski, J. Wang, H. Cha, H. Yan, K. S. Wong, G. Li, M. Li, J. Wu, *Energy Environ. Sci* **2023** *16*, 3416-3429.

[49] J. Rivnay, S. C. B. Mannsfeld, C. E. Miller, A. Salleo, M. F. Toney, *Chemical Reviews* **2012,** *112*, 5488-5519.

[50] E. Zhu, L. Fu, Y. Lu, W. Jiang, M. H. Jee, R. Liu, Z. Li, G. Che, H. Y. Woo, C. Liu, *ACS Applied Materials & Interfaces* **2022,** *14*, 7082-7092.

[51] Q. An, J. Wang, X. Ma, J. Gao, Z. Hu, B. Liu, H. Sun, X. Guo, X. Zhang, F. Zhang, *Energy & Environmental Science* **2020,** *13*, 5039-5047.

[52] M. Sumita, K. Sakata, S. Asai, K. Miyasaka, H. Nakagawa, *Polym. Bull.* **1991**, *25*, 265.

[53] L. Zhan, S. Li, Y. Li, R. Sun, J. Min, Y. Chen, J. Fang, C. Q. Ma, G. Zhou, H. Zhu, L. Zuo, H. Qiu, S. Yin, H. Chen, *Advanced Energy Materials* **2022,** *12*, 2201076.

[54] L. Zhan, S. Yin, Y. Li, S. Li, T. Chen, R. Sun, J. Min, G. Zhou, H. Zhu, Y. Chen, J. Fang, C. Q. Ma, X. Xia, X. Lu, H. Qiu, W. Fu, H. Chen, *Advanced Materials* **2022,** *34*, 2206269.

[55] T. Liu, T. Yang, R. Ma, L. Zhan, Z. Luo, G. Zhang, Y. Li, K. Gao, Y. Xiao, J. Yu, X. Zou, H. Sun, M. Zhang, T. A. Dela Peña, Z. Xing, H. Liu, X. Li, G. Li, J. Huang, C. Duan, K. S. Wong, X. Lu, X. Guo, F. Gao, H. Chen, F. Huang, Y. Li, Y. Li, Y. Cao, B. Tang, H. Yan, *Joule* **2021,** *5*, 914-930.

[56] J. Yao, T. Kirchartz, M. S. Vezie, M. A. Faist, W. Gong, Z. He, H. Wu, J. Troughton, T. Watson, D. Bryant, J. Nelson, *Physical Review Applied* **2015,** *4*.

[57] W. Shockley, H. J. Queisser, *Journal of Applied Physics* **1961,** *32*, 510-519.

[58] J. Liu, S. Chen, D. Qian, B. Gautam, G. Yang, J. Zhao, J. Bergqvist, F. Zhang, W. Ma, H. Ade, O. Inganäs, K. Gundogdu, F. Gao, H. Yan, *Nature Energy* **2016,** *1*.

[59] Y. Wang, D. Qian, Y. Cui, H. Zhang, J. Hou, K. Vandewal, T. Kirchartz, F. Gao, *Advanced Energy Materials* **2018,** *8*, 1801352.

[60] J. Hou, O. Inganäs, R. H. Friend, F. Gao, *Nature Materials* **2018,** *17*, 119-128

[61] Y. Xie, T. Li, J. Guo, P. Bi, X. Xue, H. S. Ryu, Y. Cai, J. Min, L. Huo, X. Hao, H. Y. Woo, X. Zhan, and Y. Sun, *ACS Energy Let*ters **2019**, *4*, 1196-1203.

[62] Y. Zhang, D. Liu, T. K. Lau, L. Zhan, D. Shen, P. W. K. Fong, C. Yan, S. Zhang, X. Lu, C. S. Lee, J. Hou, H. Chen, G. Li, *Advanced Functional Materials* **2020**, *30*, 1910466.

[63] Y. Cui, H. Yao, J. Zhang, K. Xian, T. Zhang, L. Hong, Y. Wang, Y. Xu, K. Ma, C. An, C. He, Z. Wei, F. Gao, J. Hou, *Advanced Materials* **2020,** *32*, 1908205.

[64] H. Hu, Z. Ren, P. W. K. Fong, M. Qin, D. Liu, D. Lei, X. Lu, G. Li, *Advanced Functional Materials* **2019**, *29*, 1900092.

[65] S. Bae, H. Zhao, Y. Hsieh, L. Zuo, N. D. Marco,1,2 Y. S. Rim, G. Li, Y. Yang, *Chem* **2016**, *1*, 197-219.